PCCP

Accepted Manuscript

ROYAL SOCIETY OF CHEMISTRY

www.rsc.org/pccp

Journal Name

ARTICLE

Received 00th January 20xx,
Accepted 00th January 20xx

DOI: 10.1039/x0xx00000x

www.rsc.org/

Synthesis of Morphology-Controlled Bismutite for Selective Applications

Thangavel Selvamani,[a] Balasubramaniam Gnana Sundara Raj,[a] Sambandam Anandan,[*,a] Jerry J Wu,[b] and Muthupandian Ashokkumar[*,c]

Bismutite ($Bi_2O_2CO_3$) possessing diverse morphologies, namely, nanosheets, nanodiscs and nanoplatelets was synthesized by a simple controllable method using bismuth nitrate pentahydrate and urea as precursors in water/ethylene glycol mixture. The as-synthesized samples showed unique physical and chemical properties, such as varying morphology, phase identification, chemical composition, surface area and surface potential. $Bi_2O_2CO_3$ nanosheets exhibited excellent adsorption capabilities for anionic dyes (acid orange 7 and methyl orange) and high photocatalytic performance for the decolorization of cationic dyes (rhodamine B and methylene blue) under simulated solar illumination. Further, the electrochemical performance of $Bi_2O_2CO_3$ nanosheets showed good capacitance properties and hence could be a potential candidate for electrode materials in energy related applications.

Introduction

In general adsorption and photocatalysis are used in wastewater treatment (environmental remediation) for the removal/degradation of inorganic (heavy metals), organic (dyes, drugs and herbicides), and biological pollutants (virus and bacteria).[1-5] Often, selective adsorption of pollutants is a major issue and hence the development of better adsorbents is an active area of research.[6] Zhu et al. successfully developed selective adsorption of cationic dyes using anionic metal-organic framework through guest-guest exchange between mixtures of aqueous dyes solution.[7] Ma et al. effectively prepared microporous anionic metal-organic framework for selective adsorption of cationic dye from a mixture of organic dyes using charge-selective separation ion exchange method.[8] Both cases comprised of topologically controlled structures. Over the past few years, innovative synthesis of various materials for dye adsorption and selective photocatalysis has been reported.[5,9-22] The defects/oxygen vacancies play an important role for adsorption and photocatalytic behavior of these materials.[10,12,16,17,22] Alternatively, oxygen-rich compounds showed better adsorption and photocatalytic properties due to their unique physicochemical properties.[18,21] Nevertheless, the photocatalytic activity of a photocatalyst depends upon band gap, surface area, surface potential and morphologies exposed facets.[23-24] Bismuth based oxides possess narrow band gap, high charge carrier efficiency with good thermoelectric properties due to overlap between 6s (Bi) and 2p (O) of valance band.[25] Moreover, bismuth containing compounds have been used in many studies.[6,17-22,24-27] Among these $Bi_2O_2CO_3$ (Bismutite) is an emergent material and used as antibacterial, photocatalyst, sensor, supercapacitor, adsorbent and precursor for Bi_2O_3.[24,26,28-41] Bismutite belongs to Sillén phase compounds demonstrating inter-layer structures with alternative polymeric cationic $(BiO)_n^{n+}$ and anionic (CO_3^{2-}) layer and has been widely used as a photocatalyst for the degradation of toxic pollutants such as organic dyes and gaseous compounds such as nitric oxide (NO).[26,29-34,40-48] Greaves *et al.* first reported the synthesis of $Bi_2O_2CO_3$ through a simple chemical method and later, several methodologies have been reported for the synthesize of bismutite with various morphologies such as microflowers, microspheres (rose, plate, pinon-like and sponge-likes, hollow), persimmon-like, nanosheets, nanotubes, egg-tart and micro/nanostructures.[28-37,42-55] Chen *et al.* reported the synthesis of bismuth micro/nanospheres by simple chemical method using ethylene glycol as a non-toxic solvent.[56] Numerous methods are available in the literature regarding size and shape controlling of $Bi_2O_2CO_3$ via solvothermal, surfactant-assisted hydrothermal and vacuum heat treatments.[57-59] The concentration of precursors (citrate ion, nitrate ion, etc.,), additives or precipitant (urea, sodium

---

[a] *Nanomaterials and Solar Energy Conversion Lab, Department of Chemistry, National Institute of Technology, Tiruchirappalli- 620 015, India. Tel: +91-431-2503639 ; Fax: +91-431-2500133 ; E-mail : sanand@nitt.edu*

[b] *Department of Environmental Engineering and Science, Feng Chia University, Taichung 407, Taiwan.*

[c] *School of Chemistry, University of Melbourne, Vic 3010,Australia, Tel: +61-3-83447090 ; Fax: +61-3-93475180 ; E-mail : masho@unimelb.edu.au*

Electronic Supplementary Information (ESI) available: (S1-S9) FT-IR spectra of nanoplatelets and nanodiscs, Adsorption profile, XRD, FESEM and FT-IR spectra's of $Bi_2O_2CO_3$ nanosheets before and after adsorption/photocatalytic processes, photographic images showing adsorption/ photocatalytic processes for dye solutions. Tables (ST1-ST5) Unit cell parameters, Calculated E_{VB}, E_{CB} from E_g Values, RR(%), adsorption capacities and comparison of adsorption profiles. See DOI: 10.1039/x0xx00000x carbonate and ammonium carbonate, etc.,) also play a major role in achieving diverse morphologies of $Bi_2O_2CO_3$.[60-63] Likewise, the effect of co-solvent (water/ethanol or water/ethylene glycol) for various other materials have been extensively studied in order to attain excellent physicochemical characteristics.[64-66] These interesting approaches have also been implemented to attain tunable properties like surface area, surface potentials, band alignment with functional morphologies.[65-69] Hence, researchers are interested to achieve multifunctional behavior with highly efficient and excellent selective applications through composition-structural engineering aspects. Until now, to the best of our knowledge, the synthesis of $Bi_2O_2CO_3$ with mixed solvent (water /ethylene glycol) has not been reported and also extensively studied for selective applications. Herein, we report on the synthesis and characterization of $Bi_2O_2CO_3$ with various morphologies through a simple and controllable method to explore their applications in dye adsorption and photocatalytic activity. In addition, the electrochemical performance of as-synthesized samples was tested to evaluate its suitability as a supercapacitor.

Experimental

Chemicals. All chemicals were of analytical grades and used without further purification. Bismuth(III) nitrate pentahydrate (ACS reagent, 98%), urea (AR Grade, 99%), acid orange 7 (AO7: 85%), methyl orange (MO; 85%), methyl red (MR), rhodamine B (Rh B; 95%), methylene blue (MB) and sodium sulfate were purchased from Sigma-Aldrich. Vulcan XC-72 and polyvinylidenefluoride (PVDF) were purchased from Fluka. N-methyl-2-pyrrolidene (NMP), ethylene glycol (≥ 99%) and nitric acid (ACS reagent) were purchased from Merck.

Synthesis of Diverse Bismutite Nanostructures. About 6.29 g of bismuth(III) nitrate pentahydrate was dissolved in 43 mL ethylene glycol which was then mixed with 33 mL of urea solution (6.05 mol dm^{-3}) in a 100 mL round bottom flask. The initial pH of the reaction mixture was 1.2, which was then adjusted to 0.9 using concentrated nitric acid (2.1 mL). Then, the reaction mixture was refluxed at 110°C for 9 h under atmospheric pressure with constant stirring. After completion of the reaction, white bismutite nanosheet powder was collected and washed with distilled water several times and then dried at 80°C for 4 h. Nanoplatelet morphology was obtained by following a similar experimental condition but without addition of concentrated nitric acid. Whereas, nanodisc morphology was obtained by refluxing at 80°C for 9 h keeping other conditions similar.

Characterization. The surface morphology was observed with field emission scanning electron microscope (FESEM model JEOL 7401F) and transmission electron microscope (TEM model JEOL JEM 2010). Chemical composition and elemental analysis were carried out using energy dispersive X-ray spectroscopy (EDS, Oxford Inc). The phase identification and crystal structures of the samples were determined by powder X-ray diffraction (XRD) using Rigaku D/max-2500 diffractometer with Ni-filtered Cu Kα radiation source (40 kV, 30 mA, λ= 1.5406 Å). Fourier transform infrared (FTIR) spectra were measured on Nicolet iS50 infrared spectrophotometer using KBr pellet technique. Micro-Raman spectra of the sample were measured by backscattering configuration using in EnSpectr RS-532 Raman system. X-ray photoelectron spectroscopy (XPS) measurements were recorded on Physical Electronics PHI 5600 spectrophotometer with monochromatic Al Kα (1486.6 eV) X-ray as excitation source. The nitrogen gas adsorption-desorption measurements were performed with Micromeritics ASAP2010 at liquid nitrogen temperature (77K) and surface area was calculated using Brunauer- Emmett-Teller (BET) equation. Surface charge (ζ-potential) of the samples was measured at different pH using Zeta-check-zeta-potential analyzer (Microtrac) apparatus. UV-visible absorption spectra (diffuse reflectance mode; DRS) were recorded using ultraviolet-visible (UV-vis) spectrophotometer (T90+, PG instruments, UK) with an integrating sphere using $BaSO_4$ as a standard. The photoluminescence (PL) spectra of the samples were performed with Shimadzu (RF5301PC) spectrofluorometer at an excitation wavelength (370 nm) under ambient conditions. The photocurrent measurement was performed by AUTOLAB12/ FRA2 in a three-electrode system as-synthesized samples coated on FTO as working electrode and platinum (Pt) counter as well as reference electrode with polymer ion gel used for solid electrolyte under xenon illumination source (150 W with standard 85 mW cm^{-2}).

Adsorption Studies. Adsorption studies were performed by magnetically stirring the mixture at room temperature (natural pH). In a typical process, 25 mg of the samples was taken in 125 ml borosilicate glass bottle which contained 100 mL of organic dye solution ($1x10^{-4}$ mol L^{-1}: AO7 and MO; $5x10^{-5}$ mol L^{-1}: MR, Rh B and MB). The suspension was constantly stirred and at regular time intervals about 4 mL aliquots of reaction mixtures were removed and filtered using PVDF syringe filter (0.45 µm) to estimate the amount adsorbed. The amount of adsorbed dyes was quantified using UV-vis spectrophotometer (T90+, PG instruments, UK). The removal ratios (RR) of adsorption for dyes was calculated using the formula (RR= $(C_0-C)/C_0* 100\%$). Then, the adsorption capacity of each dyes on the samples was calculated using $Q_m= (C_0-C)* V/m$. Here, the Q_m is adsorption capacity (mg g^{-1}), C_0 and C are concentrations of dye (mg L^{-1}) before and after adsorption, respectively, V is the volume of solution (L) and m for mass of the samples taken (g). Further, the selective adsorption of anionic dye (AO7 and MO) from a mixture (AO7 in MB and MO in MB) was studied under similar concentrations with as-synthesized samples as adsorbents.

Photocatalytic Activity. Photocatalytic experiments of the synthesized samples were carried out at natural pH under ambient atmospheric conditions using 150 W tungsten halogen lamp (λ≥400 nm; intensity of incident radiation was 80,600±10 Lux measured using Extec, USA). The samples (50 mg of catalyst) were dispersed in 125 mL borosilicate glass bottle which contained 100 mL of organic dye solution ($5x10^{-5}$ mol L^{-1}: Rh B and MB). Prior to illumination, the suspension was magnetically stirred in dark for 30 min to attain adsorption/desorption equilibrium. During irradiation, 4 mL of solution was collected at regular time intervals from the suspension mixtures and the catalyst was filtered by PVDF syringe filter (0.45 µm). The photocatalytic activity of synthesized samples was calculated by measuring the remaining concentration of organic dye using UV-vis spectrophotometer (T90+, PG instruments, UK).

Electrochemical Measurement. The working electrode was fabricated as described below: About 75 wt.% bismutite, 20 wt.% Vulcan XC-72 carbon (conductive agent) and 5 wt.% of PVDF (binder) were ground in a mortar then a few drops of NMP solution was added to form a slurry. The slurry was then coated onto a pretreated SS plate (active electrode area was 1.0 cm^2) and dried at 100 °C under vacuum for 12 h. Capacitance measurements were performed with standard three-electrode system containing above prepared SS plate as working electrode, Pt foil as a counter electrode, and Ag/AgCl as a reference electrode in 1 M Na_2SO_4 aqueous solution as electrolyte. Cyclic voltammetry (CV), galvanostatic (GV) charge–discharge and electrochemical impedance spectroscopy (EIS) techniques were performed at room temperature by using a potentiostat/galvanostat (AUTOLAB 302N module) as testing system. The supercapacitor performance of as-synthesized sample was measured at different scan rates (5, 10, 20, 40, 80 and 160 mV s^{-1}) within the potential range of −0.1 to +0.4 V. Then, a long term galvanostatic charge–discharge performance was carried out up to 1000 cycles at a current density of 0.1 mA cm^{-2} in the potential range of −0.1 to +0.4 V. The specific capacitance (SC) for as-prepared working electrodes was calculated from galvanostatic discharge curves using the Equation (1).

$$SC=\frac{It}{m\Delta E} \qquad (1)$$

where, I is current applied (amperes), t is discharging time in seconds, m is mass of the sample present on the electrode in grams and ΔE is the operating potential window in volts of charge and discharge. Further, the electrochemical impedance spectroscopic measurements were carried out in alternating current frequency range of 0.1Hz – 100 kHz at open circuit voltage with an excitation signal of 10 mV for an impedance spectrum analysis.

Results and discussion

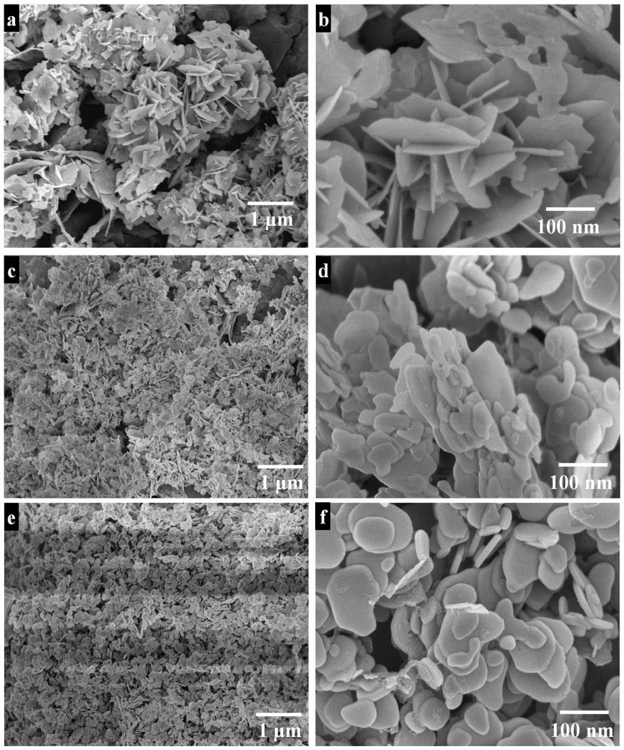

Fig. 1 Low and High magnification FESEM images of $Bi_2O_2CO_3$ nanosheets (a-b), nanoplatelets (c-d) and nanodiscs (e-f).

Microscopic Observations: Morphological features of as-synthesized sample (refluxed at 110°C for 9 h in the presence of concentrated nitric acid) are shown in Fig. 1a and 1b. Low magnification FESEM image (Fig. 1a) shows that as-synthesized sample has a sheet-like morphology. A high magnification image (Fig. 1b) shows that each sheet is about 200-300 nm in length and 5-10 nm in thickness. Whereas, platelets-like morphology (Fig. 1c and d) is seen for the preparation procedure in the absence of concentrated nitric acid. While under similar reaction conditions, upon refluxing at 80°C for 9h produced disc-like morphology with 50-100 nm diameter and 10-15 nm thickness (Fig. 1e and f). TEM results of synthesized sample (refluxed at 110°C for 9 h in the presence of concentrated nitric acid) reveal nanosheet morphology with immensely porous architecture and lateral dimension of 200-300 nm in length and 300-500 nm in width (Fig. 2a and b). The observed lattice fringe d space of 0.271 nm in HRTEM are good agreements with (110) plane of interplaner distance for nanosheets of bismutite (Fig. 2c). Further, the selected area electron diffraction (SAED) patterns of nanosheets confirm diffraction rings which are in good agreement with polycrystalline nature for tetragonal structure of bismutite (Fig. 2d). EDS spectrum (Fig. 2e) of nanosheets shows the presence of Bi, C and O elements confirming that synthesized material is pure $Bi_2O_2CO_3$.

Spectroscopic Data. Powder XRD patterns of as-synthesized samples are shown in Fig.3. All diffraction lines can be indexed to tetragonal phase of $Bi_2O_2CO_3$ which are in good agreement

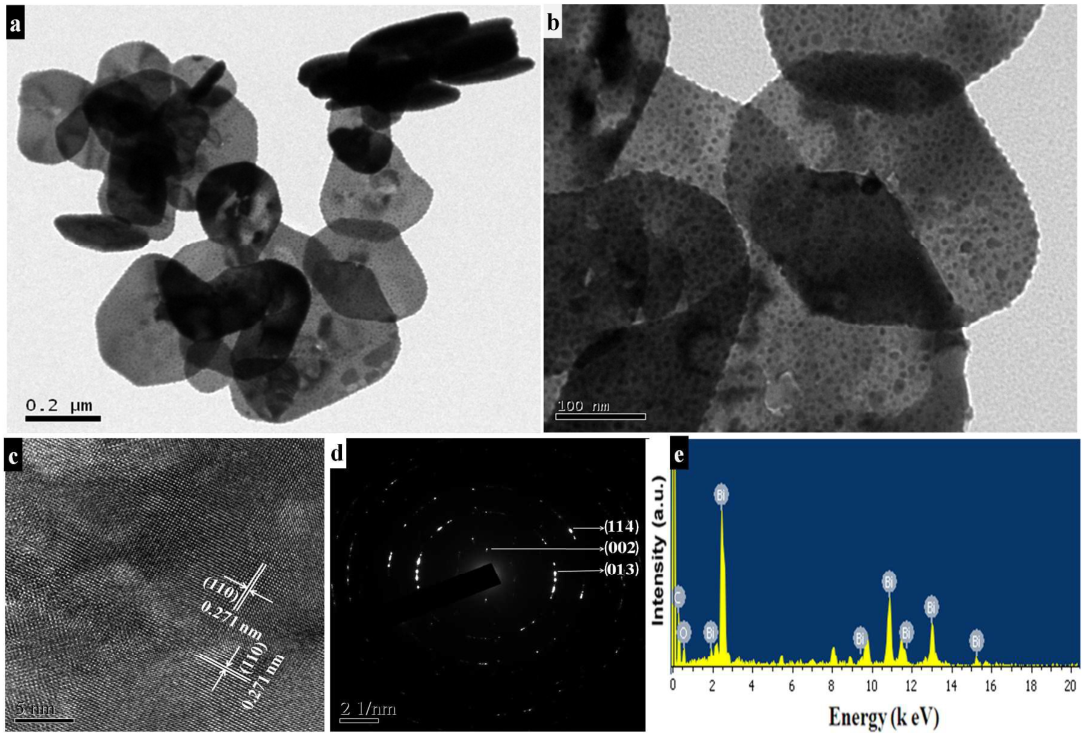

Fig. 2 TEM images (a-b), HRTEM image (c), SAED pattern (d) and EDS spectrum (e) of $Bi_2O_2CO_3$ nanosheets.

with analogous JCPDS card no. 41-1488. Here, the distinct diffraction patterns at (2θ) 30.2, 32.6 and 46.8 lines correspond to (013), (110) and (020) planes, respectively indicating the diverse nanostructures obtained during reaction process. The intensity of diffraction lines attribute to the control over different growth orientations (crystallographic direction).[17] In addition, the line broadening at 30.2 (013 plane) for nanosheets indicates smaller crystallites when compared with other morphologies. While all other morphologies show high crystallinity with pure tetragonal phase of bismutite. The crystal sizes of as-synthesized samples are found to be 24, 28 and 29 nm for nanosheets, nanodisc and nanoplatelet, respectively calculated using Debye-Scherrer's formula for the most intense line at 30.2 (013 plane). The unit cell parameters of as-synthesized samples can be calculated by least square method and given in Table ST1 (see ESI†).The FTIR spectrum of nanosheets is shown in Fig. 4a. The spectrum confirms the presence of carbonate ion (CO_3^{2-}) characteristic peaks which could be observed at 1036 cm^{-1} for symmetric vibration (ν_1), 1376 cm^{-1} and 1462 cm^{-1} (broad shoulder) for anti-symmetric vibration (ν_3), 838 cm^{-1} for outer-plane bending (ν_2) and a shoulder at 690 cm^{-1} for inner-plane deformation (ν_4).[30] Also, the additional vibration peak at 2424 cm^{-1} is attributed to the presence of carbonate ion.[43] Other peaks at 3424 cm^{-1} and 1760 cm^{-1} could be assigned to the presence of surface O-H stretching due to chemisorbed and/or physisorbed water molecules. No additional characteristic vibration peaks are observed under typical synthetic process which confirms the purity of $Bi_2O_2CO_3$. Similarly, the FT-IR spectra of nanodiscs and nanoplatelets morphologies clearly indicate the formation of highly pure $Bi_2O_2CO_3$ (Fig.S1, see ESI†). Typical Raman spectra of $Bi_2O_2CO_3$ nanosheets are shown in Fig. 4b in which the characteristic peaks of CO_3^{2-} ion are observed at 1360, 1070 and 670 cm^{-1} could be attributed to ν_3, ν_1 and ν_4 vibrations, respectively. Metal–oxygen (Bi=O) stretching vibration peak could be observed at 518 cm^{-1}. Characteristic peaks at 161, 362 and 426 cm^{-1} are also obtained due to external vibration modes for Raman analysis.[45, 70] The crystal lattice of anions (CO_3^{2-}) are hidden under the general positions (C_1) for bismutite. Therefore, all vibrational modes become active for both FTIR and Raman analysis (Degeneracies are removed).[70] Chemical state of the elements and surface compositions of as-synthesized $Bi_2O_2CO_3$ nanosheets were confirmed by XPS (as shown in Fig. 4c-f). The survey spectrum (Fig. 4c) indicates the presence of Bi, C and O elements, which are located at 160, 288 and 530 eV for chemical binding energy states, respectively. Nevertheless, the core-level XPS signal on Bi 4f element (Fig. 4d) displays two peaks at 159.0 and 164.3 eV for Bi $4f_{7/2}$ and Bi $4f_{5/2}$ which could be assigned for spin-orbit splitting of Bi^{3+} in $Bi_2O_2CO_3$ sample. Although, C 1s spectra (Fig. 4e) obviously show two characteristic peaks at 285.0 and 288.9 eV which are due to

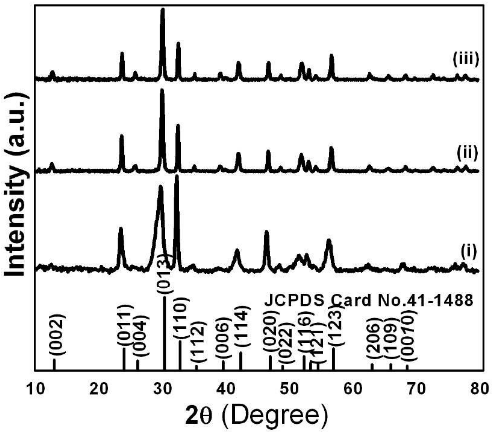

Fig. 3 Powder XRD patterns of $Bi_2O_2CO_3$ nanosheets (i), nanoplatelets (ii) and nanodiscs (iii).

carbonate ion (CO_3^{2-}). Whereas, the spectrum in Fig. 4f demonstrates O 1s state, confirmed by two peaks at 529.8 and 532.1 eV for Bi-O binding energy and carbonate ion species adsorbed with chemisorbed OH^- in water molecule on to the surface of sample, respectively.[31, 45-46] Thus, the XPS spectrum also confirms that the as-synthesized sample is highly pure.

Mechanism for Formation of Diverse Nanostructures. A schematic illustration for the formation of bismutite with diverse morphologies is shown in Scheme 1. Reactions 2-5 show the formation for $Bi_2O_2CO_3$. $Bi(NO_3)_3.5H_2O$ was dissolved in ethylene glycol to produce glycolate complex solution (A) [Reaction 2].[71] Urea solution (B) was prepared by dissolving in double distilled water. When solutions (A) and (B) were mixed and heated to 110°C, urea underwent hydrolysis to produces NH_4^+ and OH^- ions [Reactions (3) and (4)]. During the course of reaction, the glycolate complex reacted with the product to generate unique nanocrystals of $Bi_2O_2CO_3$ [Reaction (5)].

Here, ethylene glycol acts as a complexing agent as well as a co-solvent. However, the addition of concentrated nitric acid into this reaction mixtures leads to controlled complex formation between Bi(III) - EG due to the common ion effect (NO_3^-) which may affect the initial nucleation and growth to generate unique nanocrystals.[9] As a result, thinner $Bi_2O_2CO_3$ nanosheets are formed. Whereas in the absence of concentrated nitric acid, intrinsic growth of nuclei leads to plate-like morphology. Experiments performed at lower

$$Bi(NO_3)_3.5H_2O + 3HOCH_2CH_2OH \rightarrow Bi(OCH_2CH_2OH)_3 + 5\ H_2O + 3\ HNO_3 \quad (2)$$

$$CO(NH_2)_2 + H_2O \rightarrow 2NH_3 + CO_2 \quad (3)$$

$$NH_3 + H_2O \rightarrow NH_4^+ + OH^- \quad (4)$$

$$2Bi(OCH_2CH_2OH)_3 + CO_2 + 12OH^- \rightarrow Bi_2O_2CO_3 + 6(HOCH_2CH_2OH) + 3H_2O + 3O_2 \quad (5)$$

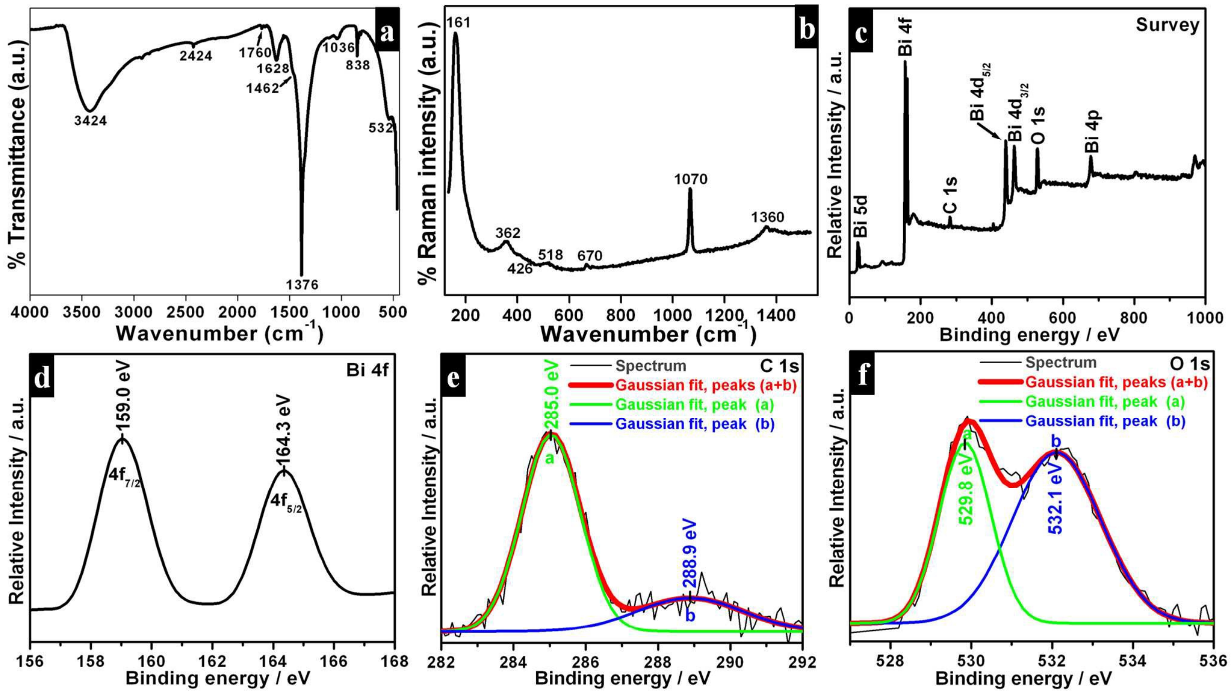

Fig. 4 FT-IR (a), Raman (b) and XPS spectrum (c-f) of $Bi_2O_2CO_3$ nanosheets.

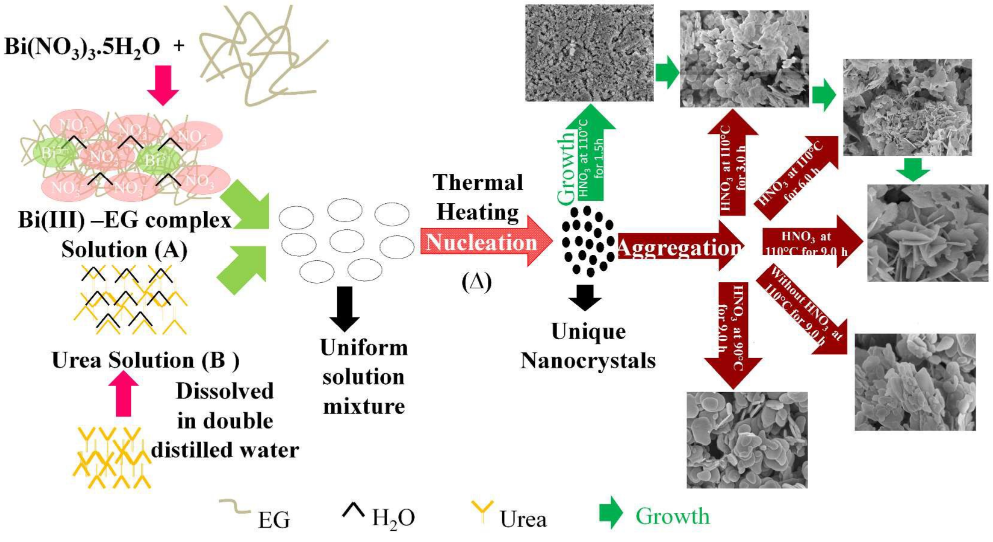

Scheme 1 Schematic illustration for the formation of diverse nanostructures of Bi$_2$O$_2$CO$_3$

temperature (80°C) leads to produce only disc-like morphology due to much slower rate of production of NH_4^+ and OH^- ions from urea hydrolysis. In order to understand the nanosheets growth process, experiments were performed at different time period (1.5, 3 and 6h) under identical conditions. The obtained samples were analyzed by both SEM and powder XRD (Fig. 5). In the case of 1.5 h experiment, the obtained product is only nanocrystals of Bi$_2$O$_2$CO$_3$, whereas in the case 3h experiment smaller nanocrystals aggregate into nanosheets-like morphology. In the case of 6h experiment nanosheet morphology is noticed due to Oswald ripping processes. Whereas, in the case of 9h experiment well developed product, i.e., Bi$_2$O$_2$CO$_3$ nanosheets having 200-300 nm in length and 5-10 nm in thick, is obtained. The powder XRD patterns also further support such nanosheet formation.

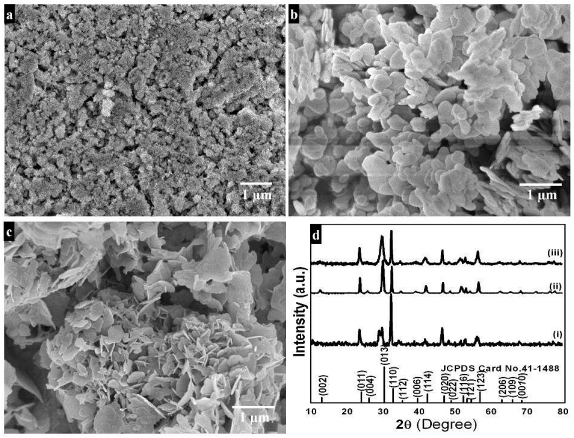

Fig. 5 FESEM images of Bi$_2$O$_2$CO$_3$ nanosheets at 1.5h (a), 3.0h (b) and 6.0h (c). Powder XRD patterns of Bi$_2$O$_2$CO$_3$ nanosheets (d) at 1.5h (i), 3.0h (ii) and 6.0 h (iii).

Surface Area, Pore Size Distributions and ζ-Potential Measurements. The nitrogen (N$_2$) adsorption-desorption isotherms and Barrett- Joyner-Halenda (BJH) pore size distribution of as-synthesized Bi$_2$O$_2$CO$_3$ nanosheets are shown in Fig. 6a. The adsorption isotherms resemble Type-III which possess macroporous surface with monolayer-multilayer adsorption. Also the adsorption hysteresis loops clearly indicate H3 type without any limiting adsorption at high P/P0 values which may be due to the existence of plate-like

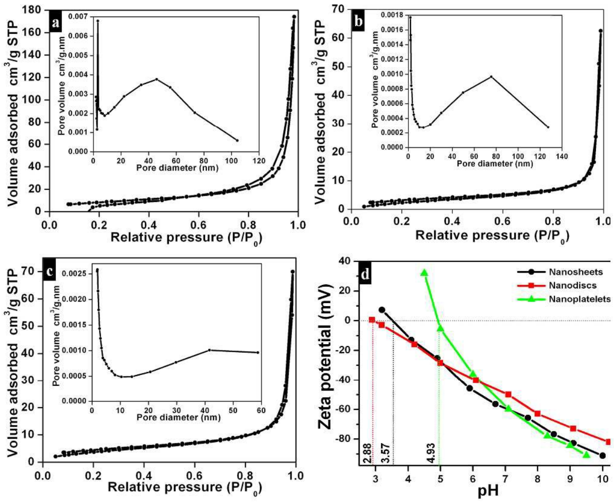

Fig. 6 Nitrogen gas adsorption/ desorption isotherm of Bi$_2$O$_2$CO$_3$ nanosheets (a), nanoplatelets (b) and nanodiscs (c). ζ-potential curve of Bi$_2$O$_2$CO$_3$ nanosheets, nanoplatelets and nanodiscs (d).

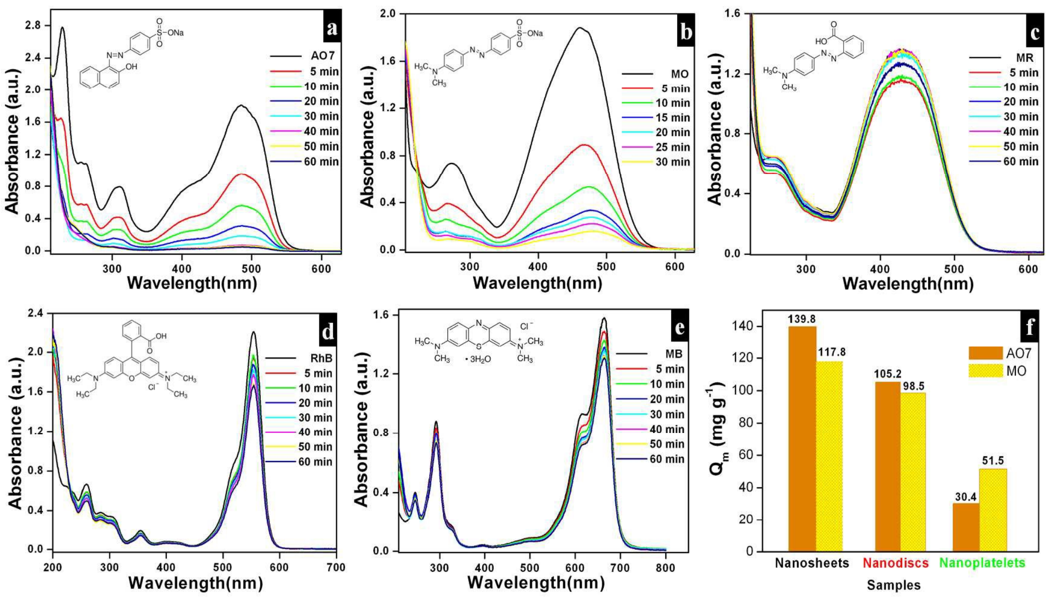

Fig.7 Time dependence UV-vis absorption spectrum of $Bi_2O_2CO_3$ nanosheets in the presence of AO7 (a), MO (b), MR (c), Rh B (d) and MB(e) under dark. Adsorption capacity profile for different morphologies of $Bi_2O_2CO_3$ in the presence of AO7 and MO (f).

particles or slit-like pores.[72-73] The calculated specific surface area of $Bi_2O_2CO_3$ nanosheets is about 30 m^2 g^{-1} calculated by Brunauer–Emmett–Teller (BET) equation. The specific surface areas of $Bi_2O_2CO_3$ nanoplatelets and nanodiscs morphologies are about 11 and 16 m^2 g^{-1}, respectively (Fig. 6b and c). The surface charges of as-synthesized $Bi_2O_2CO_3$ samples were determined by ζ-potential measurement: ζ-potential vs pH is shown in Fig. 6d. It could be seen that it is positive at low pH and negative at high pH. The isoelectric point for all samples are below pH 7.

Adsorption of dyes. The adsorption capacities of as-synthesized $Bi_2O_2CO_3$ samples were evaluated by dispersing the samples in aqueous solutions containing dyes. AO 7, MO, MR, Rh B and MB were chosen as model dye pollutants. Fig. 7 a-e show UV-vis absorption spectra of above mentioned dyes. The percentage of adsorption profile (RR) reveals that about 96% of AO 7 adsorbed on $Bi_2O_2CO_3$ nanosheets in 60 min (Fig. 7a). The spectra shown in Fig. 7b indicate that the rate of adsorption of MO on $Bi_2O_2CO_3$ nanosheets is faster than that of AO 7. However, only negligible amounts of neutral (MR) and cationic (Rh B and MB) dyes were adsorbed on as-synthesized $Bi_2O_2CO_3$ nanosheets (Fig.7 c-e). From the results, it could be suggested that $Bi_2O_2CO_3$ nanosheets exhibit selective adsorption towards anionic dyes only. Likewise experiments performed with the other morphologies (nanodiscs and nanoplatelets) show percentage of adsorption profile (RR) of about 75 and 21% towards AO 7 and 78% and 40% for MO under identical conditions (Fig. S2, see ESI†). In addition, the adsorption capacities were calculated for as-synthesized samples and illustrated in Fig. 7f (statistical plot for AO 7 and MO adsorption). Obviously, the nanosheets show enhanced adsorption capacity of AO 7 about 139.8 mg g^{-1} which is significantly high compared with nanodiscs and nanoplatelets (105.2 mg g^{-1} and 30.4 mg g^{-1}, respectively). Likewise, MO

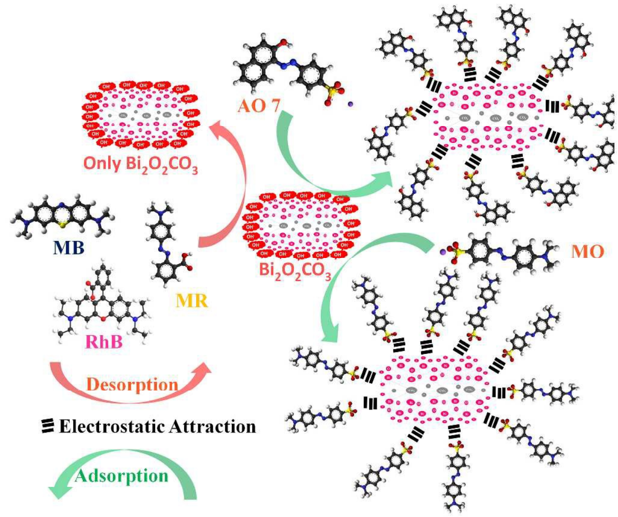

Scheme 2 Schematic representation of adsorption and desorption of dyes for as-synthesized $Bi_2O_2CO_3$ samples.

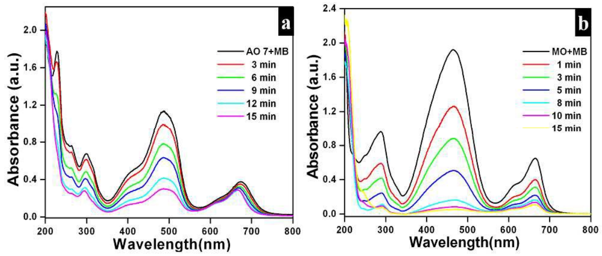

Fig. 8 (a) UV-Vis absorption spectrum of $Bi_2O_2CO_3$ nanosheets in the presence of AO 7in MB (a) and MO in MB (b).

shows higher adsorption on nanosheets (117.8 mg g^{-1}) compared to nanodiscs (98.5 mg g^{-1}) and nanoplatelets (51.5 mg g^{-1}). In order to explain the adsorption behavior of anionic, neutral and cationic dye molecules on as-synthesized $Bi_2O_2CO_3$ a possible mechanism is proposed and illustrated in Scheme 2. The observed negative ζ-potential values (-58, -49 and -59 mV for nanosheets, nanodisc and nanoplatelet) suggest that the prepared samples have OH groups adsorbed on the surface.[74-75] In the case of anionic dye, adsorption is caused by electrostatic stabilization/interaction between adsorbent (as-synthesized $Bi_2O_2CO_3$ samples) and surface OH groups (negative ζ-potential). Whilst, in the case of neutral and cationic dyes there are no such electrostatic stabilization/interactions.[9,74] Molecular and microstructural level changes have taken place upon adsorption of anionic dye which could be confirmed by FESEM (undetermined morphology), FT-IR (characteristic band changes due to structural complexation) and powder XRD results (no changes in tetragonal phase) (Fig S3, See ESI). Also experiments were carried out under identical conditions to understand preferential adsorption of certain dye in a dye mixture. In the case of AO 7 and MB dye mixtures AO7 is selectively adsorbed (Fig. 8a) whereas MO and MB dyes adsorb due to co-adsorption caused by inductive effect of dye molecules (Fig. 8b). Nevertheless, for AO7 and MB dye mixtures such inductive effect caused by MB molecule is prevented due to steric hindrance of AO 7 structure (OH functional group is in cis position towards -N=N- and intra molecular hydrogen network) whereas in MO molecular structure (-N=N- azo group is in trans position between two aromatic rings) no such steric hindrance.[9]

Photocatalytic activity and optical properties. The photocatalytic efficiencies of as-synthesized samples were evaluated using Rh B and MB (cationic dyes) as model pollutants. Fig. 9a shows absorption spectra observed for Rh B solution during photocatalytic degradation in the presence of $Bi_2O_2CO_3$ nanosheets as a photocatalyst. Upon irradiation for 240 min, the characteristic absorption peak at 553 nm for Rh B gradually decreased. The photocatalytic degradation efficiency (D) for Rh Bwas calculated using Equation (6).

$$D = (A/A_0) * 100 \qquad (6)$$

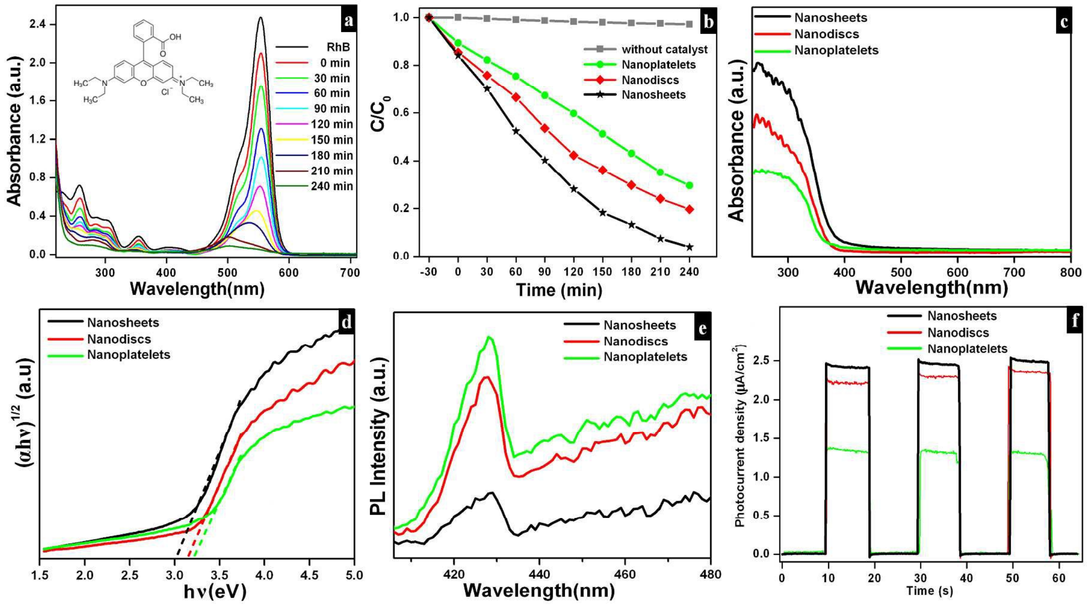

Fig. 9 Time dependence UV-vis absorption spectrum of $Bi_2O_2CO_3$ nanosheets in the presence of Rh B (a) under illumination. Photocatalytic degradation curve for different morphologies of $Bi_2O_2CO_3$ in the presence of Rh B (c). DRS absorption spectrum (d), corresponding Tauc plot (d), PL emission (e) and photocurrent responses (f) for $Bi_2O_2CO_3$ samples

where, A and A_0 are Rh B concentrations after and before degradation, respectively. For comparison, similar experiments were performed with $Bi_2O_2CO_3$ nanodiscs and nanoplatelets and as well as without any catalyst (blank test) and the results are shown in Fig. 9b. $Bi_2O_2CO_3$ nanosheets showed 98% decolorization of Rh B after 240 min under simulated solar illumination, while in the absence of photocatalyst (blank test) only 3% decolorization was observed (Fig. 9b). For $Bi_2O_2CO_3$ nanodiscs and nanoplatelets morphologies about 80 and 70% decolorization of Rh B were observed under identical conditions. The higher photocatalytic activity for Rh B decolorization under $Bi_2O_2CO_3$ nanosheets could be attributed to its high surface area (30 m^2 g^{-1}), morphology and distinct textural properties (negative ζ-potential value).[23,43] Similarly, the photocatalytic degradation of other cationic dye (MB) was performed under identical conditions using as-synthesized $Bi_2O_2CO_3$ samples as the photocatalyst (Fig. S4, see ESI†). $Bi_2O_2CO_3$ nanosheets showed 95% decolorization of MB after 600 min under illumination whereas 48 and 66 %, were observed in the case of nanoplatelets and nanodiscs, respectively (Fig. S4, see ESI†). However, the photocatalysts do not show similar catalytic activity due to molecular structure (Rh B has both partially positive and negative ions whereas MB has only positive ions).[9, 76] In addition, possible adsorption/desorption of the dye molecules with specific textural characteristic of $Bi_2O_2CO_3$ samples influence the photocatalytic process.[75] Further, the effect of photocatalytic activity was explained by facilitated optical absorption/emission characteristics (band gap/holes and electrons). The light absorption performance of $Bi_2O_2CO_3$ samples is shown in Fig. 9c. In addition absorption coefficients of as-synthesized samples were examined by Tauc plots. The optical absorption band gap of semiconductor was calculated using Equation (7).[77]

$$\alpha = \frac{C\left(\text{⍰}\nu - E_g^{bulk}\right)^{1/2}}{\text{⍰}\nu} \qquad (7)$$

where α is the absorption coefficient, C is a constant, hν is the photon energy and E_g^{bulk} is the band gap. The estimated band gaps of as-synthesized $Bi_2O_2CO_3$ samples are 3.02, 3.12 and 3.21 eV for nanosheets, nanodiscs and nanoplatelets, respectively by the extrapolation of linear region of $(\alpha h\nu)^{1/2}$ versus photon energy hν plots (Fig. 9d).[77] The emission spectra of as-synthesized $Bi_2O_2CO_3$ show strong emission peak at 428 nm (λ_{ex} =370 nm), which could be attributed to photo-generated holes and electrons on the surface (Fig. 9e).[78] The emission intensity of $Bi_2O_2CO_3$ nanosheets is less intense due to the reduction in recombination rate and separation of photogenerated carriers leading to a higher photocatalytic activity.[22] To support this, photocurrent density measurements were performed for as-synthesized $Bi_2O_2CO_3$ samples and shown in Fig (9f). $Bi_2O_2CO_3$ nanosheets obviously showed much higher photocurrent response, which implies superior photocatalytic activity than that of nanodiscs and nanoplatelets (Fig. 9f). Based on the results of these studies for photocatalytic activity, a mechanism is suggested in scheme 3. Here, the valance band (VB) and conduction band (CB) potentials of as-synthesized $Bi_2O_2CO_3$ samples can be calculated (Table ST2 (see ESI†)) using the following equations (8-9)

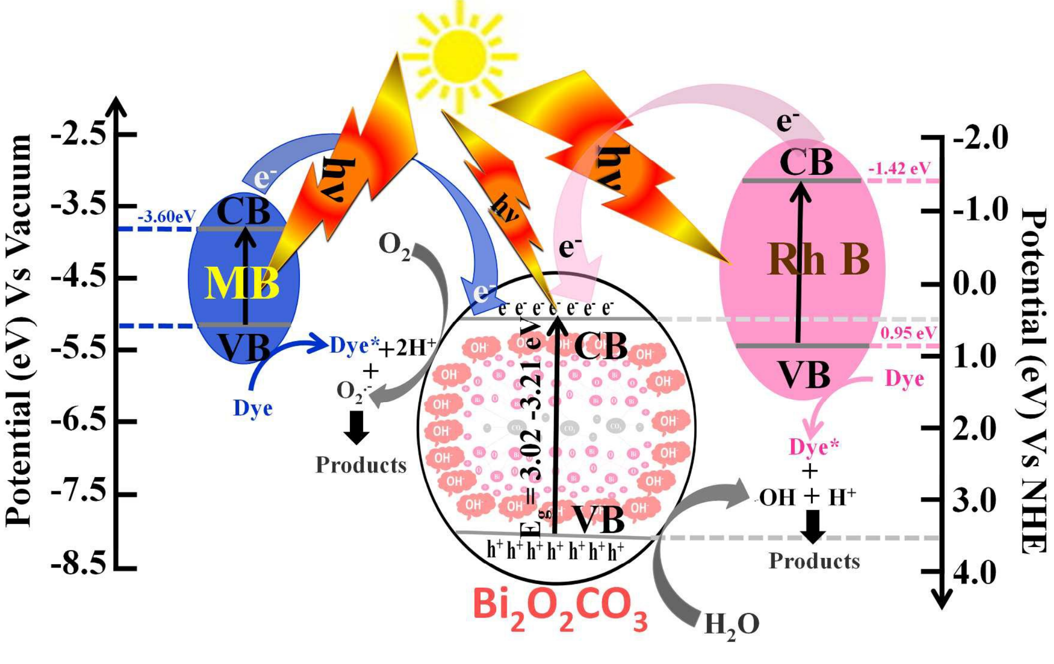

Scheme 3 Schematic demonstration showing band structure and mechanism for photocatalytic performances of dyes over as-synthesized $Bi_2O_2CO_3$ samples under simulated solar illumination

$E_{VB} = X - E_e + 0.5\ E_g$ (8)

$E_{CB} = E_{VB} - E_g$ (9)

where X is the absolute electronegativity of $Bi_2O_2CO_3$, which is defined as the geometric average of the absolute electronegativities of the constituent atoms. E_e is the energy of free electrons on the hydrogen scale (E_e= 4.5 eV). X was found to be 6.543 eV for $Bi_2O_2CO_3$. However, the positioned of CB value at 0.438 to 0.533 eV of as-synthesized $Bi_2O_2CO_3$ samples given in Table ST2 is more positive than that of $O_2/O_2^{\cdot-}$ (-0.28 eV Vs NHE) which implies photoreduction through electron and the position of $^{\cdot}OH/H_2O$ (+2.27 eV Vs NHE) displays more positive than that of VB suggesting photooxidation through holes, respectively. Meanwhile, the dye molecules are stable under simulated solar illumination (without catalyst) and presence of photocatalyst (dark condition). Under illumination, the dye is excited and leading to electron injection from the excited state of dye into CB of photocatalyst (self-sensitization degradation).[79] In general, such photosensitization of photocatalysis is limited and follows the reactions can be proposed during for photocatalytic degradation (Reactions 10-14).[80]

$\text{Dye} + h\nu \longrightarrow \text{Dye}^*$ (10)

$Bi_2O_2CO_3 + h\nu \longrightarrow Bi_2O_2CO_3\,(e_{CB}^-) + Bi_2O_2CO_3\,(h_{VB}^+)$ (11)

$H_2O + Bi_2O_2CO_3\,(h_{VB}^+) \longrightarrow Bi_2O_2CO_3 + (^{\cdot}OH + H^+)$ (12)

$O_2 + Bi_2O_2CO_3\,(e_{CB}^-) \longrightarrow Bi_2O_2CO_3 + (O_2^{\cdot-})$ (13)

$(^{\cdot}OH + H^+) + (O_2^{\cdot-}) + \text{Dye}^* \longrightarrow$ Degradation products (14)

The results of as-synthesized $Bi_2O_2CO_3$ samples indicated E_{CB} more positive potential then that of Rh B dye (CB:-1.42 eV) and highest light absorption wavelength at 553 nm in the visible region possess photo-generated electrons from the excited RhB (dye*) which leads to higher photocatalytic activity.[81] Although, the favorable light absorption of Rh B and presence of carboxylic group (-COOH) leads to interacts with surface site of photocatalyst have much more when compared with MB (unavailable functional group). Whereas, in the case of MB with CB (-3.60 eV Vs vacuum) with light absorption at 664 nm apparently slower inclusion (week self-sensitization) for photo-generated electrons from excited state and poor interaction with photocatalyst surface site leads to lower photocatalytic activity. Therefore, as-synthesized $Bi_2O_2CO_3$ samples might have higher photocatalytic activity for Rh B than MB caused by self-sensitization degradation process upon simulated solar illumination. In addition, the photocatalytic effect for dye degradation process indeed influenced their physical parameters such as band gap, surface area, surface potential and morphology of as-synthesized samples.[23] Then, the materials' sustainability and reusability were studied after photodegradation by powder XRD, FESEM and FTIR analysis and the results are shown in Fig. S5 (see ESI†).

Electrochemical Capacitance Measurement. Electrochemical performances of as-synthesized $Bi_2O_2CO_3$ samples as electrode material for supercapacitor system were examined by cyclic voltammetry. Typical cyclic voltammogramms (Fig. 10a), are

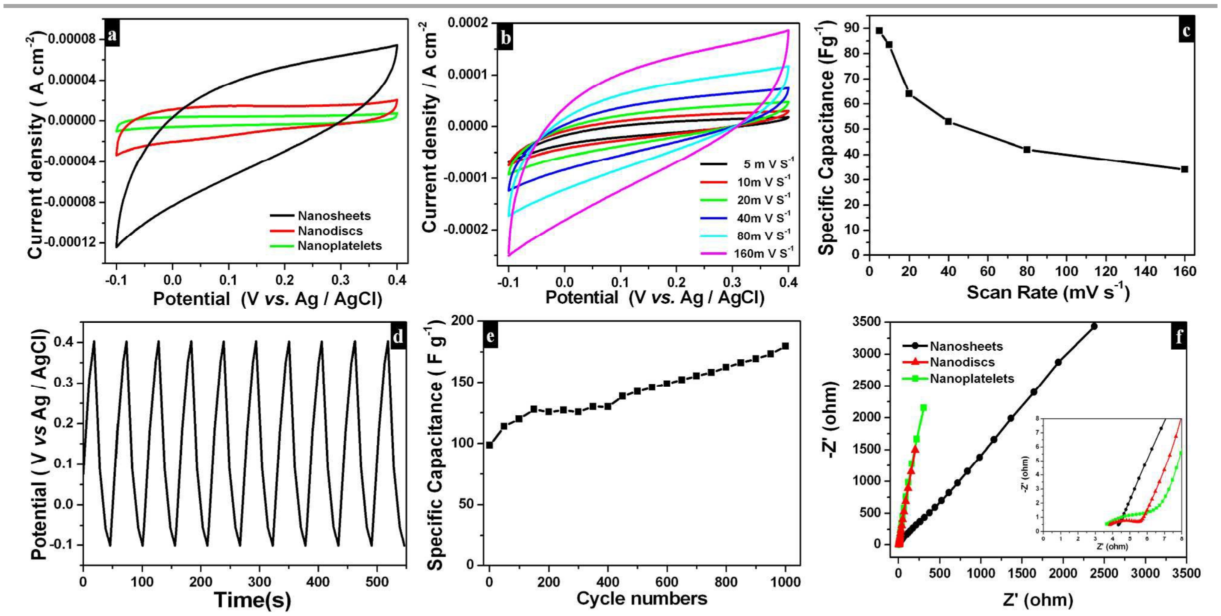

Fig. 10 CV curves (a) for different morphologies of $Bi_2O_2CO_3$ at 40 mV s-1scan rate in 1M Na_2SO_4 as electrolyte. CV curves (b) and its corresponding specific capacitance plot (c) for $Bi_2O_2CO_3$ nanosheets at different scan rates in the potential range of -0.1 to 0.4 V *vs* Ag/AgCl in aqueous solution of 1M Na_2SO_4 as electrolyte. Galvanostatic charge-discharge cycling test (d) and specific capacitances for number of cycle (d) of $Bi_2O_2CO_3$ nanosheets at the current density 0.1 mA cm^{-2}. EIS plot (f) for different morphologies of $Bi_2O_2CO_3$ at high frequency region (inset low frequency region).

measured at a scan rate of 40 mV s^{-1} with potential ranging from -0.1 to 0.4 V *vs* Ag/AgCl in 1 M Na_2SO_4 aqueous electrolyte exhibit ideal capacitive characteristic (without any redox peak currents in curves). Here, $Bi_2O_2CO_3$ nanosheets electrode show greater integrated area and very high capacitance compared to nanodiscs and nanoplatelets. At different scan rates (5, 10, 20, 40, 80 and 160 mV s^{-1}) (Fig. 10b), the current response of electrode material looks rectangular in shape with respective to the zero-current line and in addition peak current get increased with increasing scan rates which illustrates high capacitance (at low scan rate) and fast diffusion of ions (at high scan rate).[82-84] Hence, the specific capacitance of $Bi_2O_2CO_3$ nanosheets electrode decreases much low when scan rates increased as shown in Fig. 10c. Further, the GV charge-discharge behaviour of $Bi_2O_2CO_3$ nanosheets electrode were examined using chronopotentiometry (CP) (potential ranges between -0.1 to 0.4 V vs. Ag/AgCl in 1 M Na_2SO_4 aqueous electrolyte and current density 0.1 mA cm^{-2}). The charging and discharging profiles of $Bi_2O_2CO_3$ nanosheet electrodes are shown in linear variation (potential vs time plot) which indicates such material has high capacitance (Fig.10 d). The calculated specific capacitance value (83.5 F g^{-1}) for $Bi_2O_2CO_3$ nanosheets electrode get increases at higher cycles exhibit electrode surface gets activated during charging/discharging process.[85] Furthermore, the mechanistic characteristics of EIS for as-synthesized $Bi_2O_2CO_3$ samples were monitored. Fig. 10f shows the Nyquist impedance plots of as-synthesized samples exhibited a semicircle over the high frequencies and a vertical line in the low frequencies. The semicircle at high frequency range corresponds to the Faradaic charge transfer resistance (Rct), which is mainly influenced by ionic resistances of the electrolyte and electrode active material interface. The vertical line at low frequency range corresponds to ion diffusion of active electrode materials with respect to diffusive resistance at electrolyte.[85-86] Herein, $Bi_2O_2CO_3$ nanosheets electrode exhibit smaller semicircle at high frequencies region indicate charge transfer resistance decreased extremely when compared with other electrodes such as nanodiscs and nanoplatelets. Hence, as-synthesized $Bi_2O_2CO_3$ nanosheets electrode show excellent specific capacitance and good cycling stability with highly reversibility could be a promising candidate for electrode material in electrochemical supercapacitors as well as sensors and batteries applications.

Conclusions

In summary, $Bi_2O_2CO_3$ with diverse morphologies were successfully synthesized by a simple controllable method. As-synthesized samples demonstrate tetragonal structure with well crystalline nature of $Bi_2O_2CO_3$. It was observed that typical reaction parameters and reaction time provide key factor for control over the morphologies of $Bi_2O_2CO_3$ nanosheets, nanodiscs and nanoplatelets. The N_2 adsorption and ζ-potential measurements of as-synthesized samples having surface areas 30, 16 and 11 mg g^{-1} (nanosheets, nanodiscs and nanoplatelets) with negative surface charge reveals efficient adsorption of various dyes (selectively anionic dye) in aqueous solutions. Among them, $Bi_2O_2CO_3$ nanosheets have excellent adsorption capacity of 139.8 and 117.8 mg g^{-1} for acid orange 7 and methyl orange dyes, respectively. Besides, these samples exhibit remarkable photocatalytic activity for cationic dyes (rhodamine B and methyleneblue) decolorization from the aqueous solution simulated solar illumination. Further, the $Bi_2O_2CO_3$ nanosheets sample show prominent specific electrochemical capacitance of 150 F g^{-1} after 400 cycles for supercapacitor performances. Thus, as-synthesized $Bi_2O_2CO_3$ nanosheets can act as excellent materials for adsorbent and photocatalyst for wastewater treatment with supercapacitors activities for energy applications.

Acknowledgements

The research described herein was financially supported by the Department of Science and Technology, India (GITA/DST/TWN/P-50/2013) and National Science Council (NSC), Taiwan (NSC-102-2923-035-001-MY3), under the India–Taiwan collaborative research grant.

Notes and references

1 I. Ali, *Chem. Rev*. 2012, **112**, 5073-5091.
2 X. Chen, L. Liu, P. Y. Yu and S. S. Mao, *Science* 2011, **331**, 746-750.
3 H. Tong, S. Ouyang, Y. Bi, N. Umezawa, M. Oshikiri and J. Ye, *Adv. Mater*. 2012, **24**, 229-251.
4 X. Qu, J. Brame, Q. Li and P. J. J. Alvarez, *Acc. Chem. Res*. 2013, **46**, 834-843.
5 Q. Wu, X. Yang, J. Liu, X. Nie, Y. Huang, Y. Wen, J. Khan, W. U. Khan, M. Wu and T. An, *ACS Appl. Mater. Interfaces* 2014, **6**, 17730-17739.
6 F. Tian, J. Xiong, H. Zhao, Y. Liu, S. Xiao and R. Chen, *CrystEngComm*. 2014, **16**, 4298-4305.
7 Z. Zhu, Y.-L. Bai, L. Zhang, D. Sun, J. Fang and S.Zhu, *Chem. Commun.,* 2014, **50**, 14674-14677.
8 Y.-C. He, J. Yang, W.-Q. Kan, H.-M. Zhang, Y.-Y. Liu and J.-F. Ma, *J. Mater. Chem. A,* 2015, **4**, 1675-1681.
9 S. Wang, F. Teng and Y. Zhao, *RSC Adv.,* 2015, **5**, 76588-76598.
10 N. M. Tomić, Z. D. Dohčević-Mitrović, N. M. Paunivić, D. Ž. Mijin, N. D. Radić, B. V. Grbić, S. M. Aškrabic, B. M. Babić and D. V. Bajuk-Bogdanović, *Langmuir* 2014, **30**, 11582-11590.
11 A. Mills, M. Sheik, C. O'Rourke and M. McFarlane, *Appl. Catal. B; Environ.* 2009, **89**, 189-195.
12 P. Ji, J. Zhang, F. Chen and M. Anpo, *Appl. Catal. B; Environ.* 2009, **85**, 148-154.
13 S. Liang, R. Liang, L. Wen, R. Yuan, L. Wu and X. Fu, *Appl. Catal. B; Environ.* 2012, **125**, 103-110.
14 M. Lazar and W. A. Daoud, *RSC Adv.,* 2012, **2**, 447-452.
15 C. Li, M. Wei, D. G. Evans and X. Duan, *Small* 2014, **10**, 4469-4486.
16 F. Liu, Y. H. Leung, A. B. Djurišić, A. M. C. Ng and W. K. Chan, *J. Phys. Chem. C* 2013, **117**,12218-12228.
17 K. Ren, K. Zhang, J. Liu, H. Luo, Y. Huang and X. Yu, *CrystEngComm.,* 2012, **14**, 4384-4390.
18 X. Xiao, C. Liu, R. Hu, X. Zuo, J. Nan, L. Li and L. Wang, *J. Mater. Chem.,* 2012, **22**, 22840-22843.
19 F. Qin, G. Li, H. Xiao, Z. Lu, H. Sun, R. Chen, *Dalton Trans.,* 2012, **41**, 11263-11266.
20 C. F. Guo, J. Zhang and Q. Liu, *ACS Nano.* 2012, **6**, 8746-8752.
21 Q.-C. Liu, D.-K. Ma, Y.-Y. Hu, Y.-W. Zeng and S.-M. Huang, *ACS Appl. Mater. Interfaces* 2013, **5**, 11927-11934.
22 Y. Huang, H. Li, M.-S. Balogun, W. Liu, Y. Tong, X. Lu and H. Ji, *ACS Appl. Mater. Interfaces* 2014, **6**, 22920-22927.

23 M. Roy, S. Ghosh and M. K. Naskar, *Phys. Chem. Chem. Phys.,* 2015, **17**, 10160-10169.
24 F. Wang, Z. Zhao, K. Zhang, F. Dong and Y. Zhou, *CrystEngComm*. 2015, **17**, 6098-6102.
25 S. Sun and W. Wang, *RSC Adv.,* 2014, **4**, 47136-47512.
26 F. Qin, G. Li, R. Wang, J. Wu, H. Su and R. Chen, *Chem. Eur. J.* 2012, **18**, 16491-16497.
27 J. Li, Y. Y and, L. Zhang, *Nanoscale.,* 2014, **6**, 8473- 8488.
28 R. Chen, M. H. So, J. Yang, F. Deng, C.-M. Che and H. Sun, *Chem. Comm.,* 2006, 2265-2267.
29 Y. Zheng, F. Duan, M. Chen and Y. Xie, *J. Mol. Catal. A: Chem.* 2010, **317**, 34-40.
30 F. Dong, W.-K. Ho, S. C. Lee, Z. Wu, M. Fu, S. Zou and Y. Huang, *J. Mater. Chem.,* 2011, **21**, 12428-12436.
31 P. Madhusudan, J. Zhang, B. Cheng and G. Liu, *CrystEngComm.,* 2013, **15**,231-240.
32 T. Selvamani, A. M. Asiri, A. O. Al-Youbi and S. Anandan, *Mater. Sci. Forum.* 2013, **764**, 169-193.
33 T. Xiong, F. Dong and Z. Wu, *RSC Adv.,* 2014, **4**, 56307-56312.
34 Z. Zhao, Y. Zhou, F. Wang, K. Zhang, S. Yu and K. Cao, *ACS Appl. Mater. Interfaces* 2015, **7**, 730-737.
35 H. Huang, J. Wang, F. Dong, Y. Guo, N. Tian, Y. Zhang and T. Zhang, *Cryst. Growth. Des.* 2015, **15**, 534-537.
36 Y. Zhou, H. Wang, M. Sheng, Q. Zhang, Z. Zhao, Y. Lin, H. Liu and G. R. Patzke, *Sens. Actuators B* 2013, **188**, 1312-1318.
37 S. Peng, L. Li, H. Tan, Y. Wu, R. Cai, H. Yu, X. Huang, P. Zhu, S. Ramakrishna, M. Srinivasan and Q. Yan, *J. Mater. Chem. A,* 2013, **1**, 7630-7638.
38 D. Barreca, F. Morazzoni, G. A. Rizzi, R. Scotti and E.Tondello, *Phys. Chem. Chem. Phys.,* 2001, **3**, 1743-1749.
39 X. Zhang, Y. Zheng, D. G. McCulloch, L. Y. Yeo, J. R. Friend and D. R. MacFarlane, *J. Mater. Chem. A,* 2014, **2**, 2275-2282.
40 H.- Y. Jiang, P. Li, G. Liu, J. Ye and J. Lin, *J. Mater. Chem. A,* 2015, **3**, 5119-5125.
41 J. Eberl and H. Kisch, *Photochem. Photobiol. Sci.,* 2008, **7**, 1400-1406.
42 P. Taylor, S. Sunder and V. J. Lopata, *Can. J. Chem.* 1984, **62**, 2863-2873.
43 H. Cheng, B. Huang, K. Yang, Z. Wang, X. Qin, X. Zhang and Y. Dai, *ChemPhysChem.* 2010, **11**, 2167-2173.
44 L. Chen, R. Huang, S.- F. Yin, S- L. Luo and C- T. Au, *Chem. Eng. J.* 2012, **193-194**, 123-130.
45 F. Dong, S. C. Lee, Z. Wu, Y. Huang, M. Fu, W- K. Ho, S. Zou and B. Wang, *J. Hazard. Mater.* 2011, **195**, 346-354.
46 F. Dong, Y. Sun, M. Fu, W- K. Ho, S. C. Lee and Z. Wu, *Langmuir*. 2012, **28**, 766-773.
47 F. Dong, A. Zheng, Y. Sun, M. Fu, B, Jiang, W- K. Ho, S. C. Lee and Z. Wu, *CrystEngComm.,* 2012, **14**, 3534-3544.
48 F. Dong, Y. Sun, W- K. Ho and Z. Wu, *Dalton Trans.,* 2012, **41**, 8270-8284.
49 F. Dong, J. Bian, Y. Sun, T. Xiong and W. Zhang, *CrystEngComm.,* 2014, **16**, 3592-3604.
50 Y. Liu, Z. Wang, B. Huang, K. Yang, X. Zhang, X. Qin and Y. Dai, *Appl. Surf. Sci.* 2010, **257**, 172-175.
51 R. Chen, G. Cheng, M. H. So, J. Wu, Z. Lu, C- M. Che and H.Sun, *Mater. Res. Bull*. 2010, **45**, 654-658.
52 X- F. Cao, L. Zhang, X- T. Chen and Z- L. Xue, *CrystEngComm.,* 2011, **13**, 1939-1945.
53 T. Zhao, J. Zai, M. Xu, Q. Zou, Y. Su, K. Wang and X.Qian, *CrystEngComm.,* 2011, **13**, 4010-4017.
54 F. Dong, Q. Li, W. Zhang, M. Guan, W- K, Ho and Z. Wu, *Mater. Chem. Phys.* 2013, **142**, 381-386.
55 L. Yang, Q. Han, J. Zhu and X. Wang, *Mater. Lett.* 2015, **138**, 235-237.
56 G. Cheng, J. Wu, F. Xiao, H. Yu, Z. Lu, X. Yu and R. Chen, *Mater. Lett.* 2009, **63**, 2239-2242.
57 G. Cheng, H. Yang, K. Rong, Z. Lu, X. Yu and R. Chen, *J. Solid State. Chem*. 2010, **183**, 1878-1883.
58 H. Y. Liang, Y. X. Yang, J. C. Tang, M. Ge, *Mater. Sci. Semicond. Process*, 2013, **16**, 1650-1654.
59 F. Dong, T. Xiong, Y. Sun, H. Huang and Z. Wu, *J. Mater. Chem. A.* 2015, **3**, 18466-18474.
60 J. Tang, H. Zhao, G. Li, Z. Lu, S. Xiao and R. Chen, *Ind. Eng. Chem. Res.* 2013, **52**, 12604-12612.
61 S. Liu, Y. Tu and G. Dai, *Ceram. Int*. 2014, **40**, 2343-2348.
62 W. Cen, T. Xiong, C. Tang, S. Yuan and F. Dong, *Ind. Eng. Chem. Res*. 2014, **53**, 15002-15011.
63 F. Dong, H. Liu, W- K. Ho, M. Fu and Z. Wu, *Chem. Eng. J.* 2013, **214**, 198-207.
64 C- M. Lan, S- E. Liu, J- W. Shiu, J- Y. Hu, M- H. Lin and E. W- G. Diau, *RSC Advances*, 2013, **3**, 559-565.
65 T. Selvamani, T. Yagyu, S. Kawasaki and I. Mukhopadhyay, *Catal. Commun*. 2010, **11**, 537-541.
66 T. Selvamani, C. A. Manjula, S. Anandan, A. M. Asiri and M. Ashokkumar, *Cryst. Res. Technol*, 2015, **50**, 143-149.
67 H. Huang, K. Xiao, S. Yu, F. Dong, T. Zhang and Y. Zhang, *Chem. Commun.* 2016, **52**, 354-357.
68 L. Shan, G. Wang, D. Li, X. San, L. Liu, L. Dong and Z. Wu, *Dalton. Trans.* 2015, **44**, 7835-7843.
69 H. Huang, X. Li, J. Wang, F. Dong, P. K. Chu, T. Zhang and Y. Zhang, *ACS Catal*. 2015, **5**, 4094-4103.
70 G. E. Tobon-Zapata, S. B. Etcheverry and E. J. Baran, *J. Mater. Sci. Lett*. 1997, **16**, 656-657.
71 X. Xiao, R. Hu, C. Liu, C. Xing, C. Qian, X. Zuo, J. Nan and L.Wang, *Appl. Catal. B; Environ*. 2013, **140-141**, 433-443.
72 K. S. W. Sing, D. H. Everett, R. A. W. Haul, L. Moscou, R. A. Pierotti, J. Rouquérol and T. Siemieniewska, *Pure & Appl. Chem.* 1985, **57**, 603-619.
73 K. Kaneko, *J. Membrane. Sci,* 1994, **96**, 59-89.
74 C. Pan, J. Xu, Y. Chen and Y. Zhu, *Appl. Catal. B; Environ*. 2012, **115-116**, 314-317.
75 S. Obregón and G. Colón, *J. Mol. Catal. A: Chem*. 2013, **376**, 40-47.
76 Y. Lei, G. Wang, S. Song, W. Fan, M. Pang, J. Tang and H. Zhang, *Dalton. Trans.,* 2010, **39**, 3273-3278.
77 S. Anandan, G.-L. Lee, P.- K. Chen, C. Fan and J. J. Wu, *Ind. Eng. Chem. Res.* 2010, **49**, 9729-9737.
78 N. Liang, J. Zai, M. Xu, Q. Zhu, X. Wei and X. Qian, *J. Mater. Chem. A,* 2014, **2**, 4208-4216.
79 D- H. Wang, G- Q. Gao, Y- W. Zhang, L- S. Zhou, A- W. Xu and W. Chen, *Nanoscale*, 2012, **4**, 7780-7785.
80 M. Xiong, L. Chen, Q. Yuan, J. He, S- L. Luo, C- T. Au and S- F. Yin, *Dalton. Trans.* 2014, **43**, 8331-8337.
81 J. Tang, D. Li, Z. Feng, Z. Tan and B. Ou, *RSC Adv.,* 2014, **4**, 2151-2154.
82 B. G. S. Raj, R. N. R. Ramprasad, A. M. Asiri, J. J. Wu and S. Anandan, *Electrochim. Acta*. 2015, **156**, 127-137.
83 D. Wang, Q. Wang and T.Wang, *Nanotechnology*. 2011, **22**, 135604.
84 M. Toupin, T. Brousse and D. Bélanger, *Chem. Mater*. 2002, **14**, 3946-3952.
85 W. Sugimoto, H. Iwata, Y. Yasunaga, Y. Murakami and Y.Takasu, *Angew. Chem*. 2003, **115**, 4226-4230.
86 Y. Liu, W. Wang, Y. Wang, Y. Ying, L. Sun and X. Peng, *RSC Adv.,* 2014, **4**, 16374-16379.